

Nozzle Geometry Effects on Primary Atomization

M. Arienti*,

Sandia National Laboratories, Livermore, CA 94550, USA

marient@sandia.gov,

M. Sussman

Florida State University, Tallahassee, FL 32306, USA

sussman@math.fsu.edu

Abstract

The increasing demand for predictive simulations of primary atomization (the complex process of spray formation right after the injection of liquid fuel) suggests pushing the inlet boundary condition upstream of the injection hole, so that effects due to the nozzle geometry can be properly included. In this work, we address the coupling between internal (with respect to the injection hole) and external flow, in relation to the spray characteristics of primary atomization. A simulation capability is presented where internal and external flow can be seamlessly calculated across the injection hole. The injection is assumed to be sub-critical, so that the external liquid-gas interface can be handled by the combined level-set volume-of-fluid (CLSVOF) method. The solid wall boundary is represented by a second level-set function ψ on the same Cartesian, block-structured grid. A grid cell belongs to the physical flow domain if $\psi > 0$. Cells that are near the wall boundary, but outside of the flow domain, form a narrow band of ghost cells where velocity boundary conditions are assigned. Assuming no cavitation, results from the calculation of a scaled-up, transparent, six-hole Diesel nozzle are compared to experimental observations. Flow field features appearing just before the liquid is injected are highlighted, and their impact on spray characteristics is briefly discussed.

Introduction

Automotive engines must meet increasingly stringent emission and fuel consumption demands, and efficiency improvements to the fuel injection system is one key to achieve this objective. However, lack of fundamental knowledge of the injection process is currently limiting the potential for future injector designs. In particular demand is a clearer understanding of the physical processes involved as liquid fuel exits an injector. With this knowledge one could more effectively design the ideal combustible air/fuel distribution within a given combustion system, and therefore significantly improve engine performance using available technologies.

Primary breakup is the initial phase of liquid fragmentation to form droplets, ligaments or network structures. A liquid stream or sheet undergoes breakup by various modes that are classified by the Reynolds, Weber and Ohnesorge dimensionless ratios. The breakup of a high speed jet is more likely to fall within the turbulent atomization regime, where the exact physical processes leading to fragmentation are currently unclear. Experimental spray test rigs and measuring probes can be used to investigate primary breakup at the nozzle tip, however micro-meter and nano-second resolutions are required. Moreover, the dense spray region is very difficult to penetrate. This difficulty is compounded in the study of the internal flow of an injector, which cannot be optically accessed in most devices. On the other hand, the fuel internal flow provides the boundary conditions for the simulation of primary atomization: a spray calculation cannot be expected to be predictive if these conditions are not properly captured.

The numerical method used in this study has been validated in the case of simple jets, either subject to gas crossflow [1] or impinging on each other [2]. These studies calculated primary atomization from first principles (no calibration or sub-grid models); even without an explicit threshold to make the simulation fully resolved [3], they favorably compared with the droplet size statistics derived from experimental measurements. In those simulations, however, simple inlet velocity profiles were assigned, under the assumption that internal flow characteristics had limited effects on primary atomization. The new element in this paper is that we push the inlet boundary condition upstream of the injection hole to include the tip of a diesel injector. Computationally, this requires the definition of a second level set function that represents the injector's walls: this approach allows the treatment of complex shapes without sacrificing the efficient block-structured hierarchical structures that tracks the liquid surface or without implementing cut cells.

Numerical aspects of this embedded solid boundary algorithm will be described next. The method is verified on a single-phase crossflow over a half cylinder at a low Reynolds number. In these conditions, the vorticity field arising from the interaction with the curved wall can be compared with the results from more specialized, higher-order methods from the literature. The embedded solid boundary technique is shown to be free from staircase artifacts and its convergence to be at least first-order.

For the main demonstration simulation, we take advantage of the large amount of flow data on diesel injectors that has been made available by the group of M. Gavaises: Reference [4] provides an account of about ten years of experimental work in this field. In this paper we consider an early study [5] where the velocity field inside a transparent injector was measured with a laser Doppler velocimeter (LDV). Since the the flow area interrogated by the LDV must be large enough relative to the control volume of the laser beams, a scaled-up model of a Bosch six-hole vertical diesel injection nozzle was used in the experiment. Unfortunately, the test liquid was collected in a closed-loop rig instead of being injected, so no data are available on the spray characteristics. However, both simulation and experiment show a non-uniform velocity profile at the hole exit, due to the sharp turn imposed to the flow entering the hole: the resulting asymmetric spray is briefly investigated.

Numerical Method

The Navier-Stokes equations for incompressible flow of two immiscible fluids (such as a liquid/gas system) are solved with the one-fluid approach according to the level-set equations for multiphase flow [6]:

$$\rho(\phi) \frac{D\mathbf{u}}{Dt} = -\nabla p + 2\nabla(\mu(\phi)\mathbf{D}) - \sigma\kappa \nabla H(\phi) \quad (1)$$

$$\nabla \cdot \mathbf{u} = 0 \quad (2)$$

$$H(\phi) = \begin{cases} 1 & \phi \geq 0 \\ 0 & \phi < 0 \end{cases} \quad (3)$$

$$\rho(\phi) = \rho_L H(\phi) + \rho_G(1 - H(\phi)) \quad (4)$$

$$\mu(\phi) = \mu_L H(\phi) + \mu_G(1 - H(\phi)) \quad (5)$$

$$\frac{D\phi}{Dt} = 0. \quad (6)$$

In the equations above, \mathbf{u} is the vector field, p the pressure, ϕ the level-set function, and \mathbf{D} the deformation tensor, $\mathbf{D} = (\nabla \mathbf{u} + (\nabla \mathbf{u})^T)/2$; H is the Heaviside function and D/Dt the material derivative; σ is the surface tension coefficient. Buoyancy effects are neglected in this study and not included in the momentum equation.

In the coupled level-set/volume-of-fluid (CLSVOF) method, the advection equation for the liquid volume fraction,

$$\frac{DF}{Dt} = 0, \quad (7)$$

is solved in step with ϕ so that the level-set can be re-initialized in a local mass-preserving fix where F is used with the interface normals from ϕ to construct a volume-preserving distance function. The smooth zero level of ϕ represents the time-evolving interface. Its curvature is calculated with second-order accuracy from the volume fractions by the method of height fractions. The properties of density, ρ , and dynamic viscosity, μ , are function of ϕ everywhere in the computational domain.

The calculation can be carried out using block-structured, adaptive mesh refinement (AMR). Starting from the base level, boxes (with a minimum size of, say, 32^3 cells) are combined to cover all the tagged cells within assigned coverage efficiency. This set of blocks with the same grid spacing forms level 1. The refinement ratio between two consecutive refinement levels is two. The new level can in turn be tagged for refinement, and the process is repeated until the input grid resolution is achieved. Data on the fine level are either copied from a previous time step or, when the grid structure has changed locally, conservatively interpolated from the underlying coarse level. The liquid-gas interface, however, is always embedded in the finest grid level to avoid gross interpolation errors.

In a time step, the calculation is carried out on all levels, and the updated data on a fine level are averaged to the underlying coarser one. The solution proceeds via the projection method for incompressible flow. The multi-grid preconditioned conjugate gradient method (MGPCG) is adopted for solving the sparse matrix system that results from discretizing the pressure correction equation with discontinuous coefficients. Compared to the previous studies [1, 2], this work takes advantage of a new MGPCG method [7] specifically developed for the adaptive hierarchy of grids it is solved on. With an optimal blocking factor, it is found that the new MGPCG AMR method no longer consumes the majority of CPU time in comparison to the level set re-initialization step as the number of adaptive levels increases.

The non-linear advection terms in Equation (1) are calculated in non-conservative, semi-Lagrangian unsplit form. A second velocity field for the liquid phase is extrapolated to the gas phase to advect the VOF function [8]. The liquid velocity is numerically divergence-free in the liquid region, but not necessarily divergence-free in the

gas region, and this might cause small over- or under-shoots in the VOF function. A full account of the CLSVOF interface capturing method and of the multiphase flow solver developed by Sussman can be found elsewhere [8, 9], together with verification studies of surface tension-driven oscillations of a spherical drop and of ligament pinch-off induced by capillary instability.

In this Cartesian framework, the internal flow of an arbitrarily complex injector geometry is calculated by imposing a no-flux boundary condition on the body. The embedded solid boundary approach introduces a second, independent, signed distance function ψ to represent the body. The field ψ is positive outside the body and negative inside it, and its magnitude is the minimal distance between the position of ψ and the surface of the body. The solid body distance function is calculated from a surface tessellation of the injector, which needs to be provided separately. The point distance calculation is swept over all the triangles comprising the body surface, and must account for the possibility that the minimal distance occur either at the corners of triangle, along the edges of triangle, or inside the triangle. Green's theorem is used to indicate whether a point is inside or outside the body, and then the shortest distance from the point to the surface of the body is calculated. Once the area and volume fractions of computational cells at the solid boundary have been calculated, they are used in the projection of the velocity onto a solenoidal field. Through the Poisson equation and the projection operator, the components of flow velocity at the wall are made consistent with the no-slip boundary condition [10].

Verification

A verification problem for which there is a large pool of numerical and experimental results is the calculation of the two-dimensional flow around a circular cylinder of radius r . The purpose of this step is to show that the embedded solid boundary technique does not generate artifacts and that the convergence is at least first-order. Flow in the far field is assumed to be the uniform, $u = U_\infty$ for $t > 0$. The Reynolds number is defined as $Re = 2rU_\infty/\nu$. The cylinder, of radius 0.5, is located at $x = 10$. The 6×18 computational domain is formed by uniformly subdivided Cartesian cells. Medium and fine grid resolutions are obtained by halving Δx in both coordinate directions, starting from the coarsest grid of 64×192 cells. They are then compared to the reference solution, calculated with 512×1536 cells. To avoid interpolation approximations, the three solutions are decimated by a factor of 2, 4, and 8, so that the solution differences can be evaluated on the grid points of the coarsest mesh.

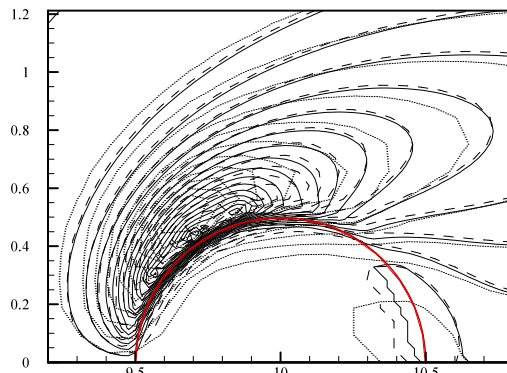


Figure 1. Contours of vorticity around a half-cylinder in crossflow at $Re = 20$. The contours, from -6 to 0 in steps of 0.2, are superimposed to the zero solid level-set line (in red), which represents the boundary of the cylinder. The dotted, dashed and continuous lines correspond to the coarse ($64/6$ cells per unity length), intermediate ($128/6$) and fine resolution ($256/6$).

The first calculation is carried out at $Re = 20$. A close-up of the contours of vorticity around the half-cylinder, both inside and outside the solid boundary, is shown in Figure 1. The zero iso-contour of the solid level-set corresponds to the red line. No spurious effects due to the embedded boundary implementation are observable, and the plot qualitatively agrees with the one obtained by Calhoun [11].

The convergence properties of the calculation are displayed in Figure 2. In order to isolate the effect of the embedded boundary method from other possible sources of error, the error norms are evaluated only on the $3\Delta x$ band of cells from the zero solid level set. For vorticity (filled symbols in Figure 2), the L_2 and L_1 difference norms decrease linearly with the grid resolution, while L_{inf} is slightly less than linear. The convergence is more than linear for the two components of velocity.

The last element of this test is the evaluation of the reattachment length L from the cylinder's trailing edge. Values at $Re = 20$ and $Re = 40$, for which a steady solution still exists, are listed on Table 1 as a function of grid spacing. They are compared with the results by Dennis & Chang [12] and by Calhoun [11]: we find that, within

the range of variation of those two results, the present calculations slightly over-estimate L , more so at the higher Reynolds number.

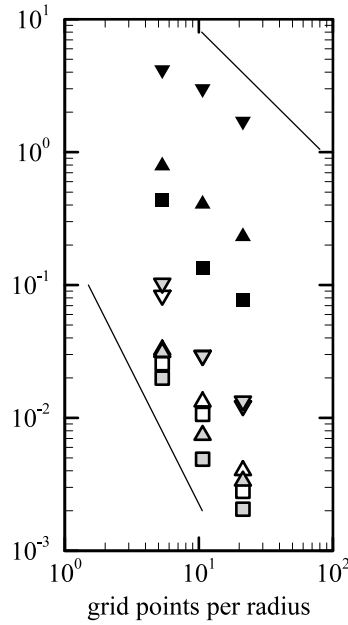


Figure 2. Convergence study for a half-cylinder in crossflow for $Re = 20$. The differences with respect to the reference solution are expressed as L_{\inf} (down triangle), L_2 (up triangle) and L_1 (square) norms for vorticity (filled symbols) and for the horizontal and vertical components of velocity (empty and grayed symbols). The two continuous lines are the linear and quadratic rate of decrease.

Δx	0.09375	0.04688	0.02344	0.01172	Dennis & Chang [12]	Calhoun [11]
L ($Re = 20$)	0.825	1.076	0.990	1.008	0.94	0.91
L ($Re = 40$)	2.130	2.633	2.419	2.458	2.35	2.18

Table 1. Reattachment length L evaluated from the cylinder's trailing edge as a function of grid spacing.

Results and Discussion

The injector for the demonstration calculation is the scaled-up Bosch six-hole diesel nozzle by Arcoumanis et al. [5]. The nozzle was manufactured at a 20:1 scale to allow flow measurements inside the sac volume and the injection holes; the nominal hole size of the model was 3.52 mm, which corresponds to a hole size of about 0.176 mm in the real injector. The conical element (the needle) was placed at 6 mm above its seat, at the maximum lift of the second stage of a real size two-stage injector. The working fluid had a density and kinematic viscosity of 893 kg/m³ and 1.64×10^{-6} m²/s, respectively. The surface tension coefficient was 0.024 N/m.

Figure 3 displays a partial schematics of the experiment. Although gravity effects are not included in our simulation, it will be convenient in the discussion to refer to an upper or lower part of the nozzle. LDV measurements were taken in vertical planes across the injection hole; the planes were located at 9.5, 10.5, 13.5 and 16.5 mm from the axis of symmetry of the nozzle. The measured flow rate of the 6 mm lift nozzle was 5.8×10^{-4} m³/s, corresponding to an average injection velocity of 10.2 m/s in the cylindrical tube. Based on this velocity and the hole diameter, the Reynolds number was approximately 2×10^4 – corresponding to an injection velocity of approximately 300 m/s in the real size nozzle. While dynamic similarity (same Re) holds for the scaled-up experiment, the cavitation number cannot be matched to the real injector's value: cavitation effects are therefore conveniently absent in this study. The measured pressure drop across the transparent nozzle was 0.85 bars, giving a total discharge coefficient of the needle seat and injection holes of 0.78.

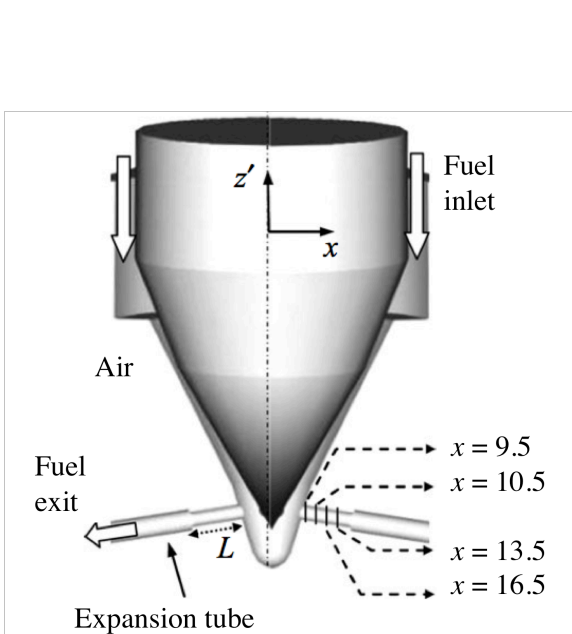


Figure 3. Configuration of up-scaled injector experiment.

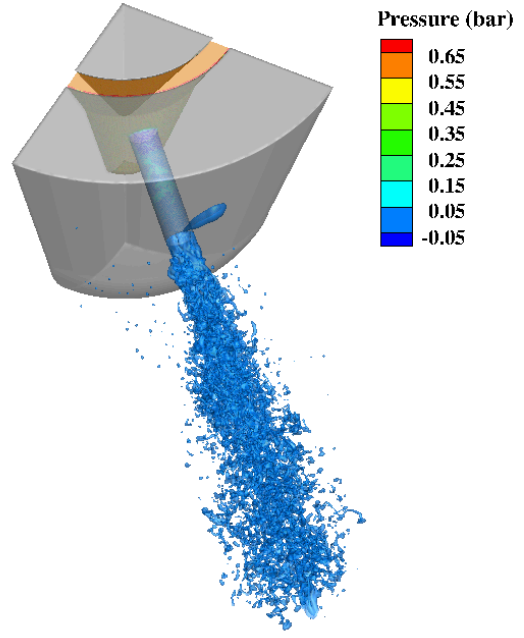


Figure 4. Simulation snapshot (at time $t = 35$ ms) of the terminal tip of the injector.

A snapshot of the CLSVOF simulation is shown in Figure 4. An important difference with respect to the experimental setup is the absence of the expansion tubes, displayed in Figure 3, that collect the test liquid after it passes the orifice (in the experiment, the test liquid was kept in a closed-loop flow rig). In the simulation, the liquid is injected instead into air at standard conditions. While this setting affects the exit velocity of the jet, it has the advantage of showing the direct link between spray characteristics and nozzle internal flow.

To reduce the computational cost, the simulation includes only a quarter of the injector and one of the six orifices. The inlet boundary velocity, applied along the open annulus at the upper boundary in Figure 4, is therefore adapted to deliver a sixth of the mass flow rate reported in the experiment. The computational domain of $100 \times 100 \times 40$ mm is sufficiently large to include the development of the jet for several orifice diameters downstream of the orifice exit. With a coarse mesh of $80 \times 80 \times 32$, the four levels of adaptive refinement used in the simulation provide the finest grid resolution of 0.0781 mm in the liquid phase. The injector walls are formed by a triangular mesh of 28,814 elements; the smallest grid size there is 0.4 mm.

At the start of the simulation, the nozzle internal cavity is almost completely filled. Afterwards, a few larger drops can be observed in the initial build-up of the jet – one large drop remains attached the injector's wall in Figure 4. The jet undergoes atomization approximately two orifice diameters downstream of the hole, and from there a complex network of ligaments and drops rapidly consumes the liquid core.

Looking upstream of the injection hole, a pressure drop of approximately 0.75 bar is found through the portion of the nozzle included in the calculation. As noted in the original experiment, the highest flow velocities in the internal flow occur at the upper corner of the hole inlet, where the lowest fluid pressures can be expected. A recirculation zone there stretches downstream from the corner over a length of more than one half of the injection hole length and occupies roughly the upper third of the hole diameter. Further downstream, the recirculation zone disappears and the velocity profile is more distributed over the hole section.

Unsteady flow is generated as a result of the sharp corner turning. For comparison we refer to the Reynolds-Averaged Navier-Stokes (RANS) solution reported in [5], where turbulence was simulated by the two equation k- ϵ model on a much coarse, co-located, non-uniform, non-orthogonal numerical grid. The time-averaged vector field from the RANS solution is displayed in Figure 5a and compared to an instantaneous snapshot of the present simulation, in Figure 5b. Note that in the latter frame the vector field is decimated in a 1:20 and that the continuum black line is the intersection of the $\psi = 0$ iso-contour with the slicing plane. Examination of similar snapshots from the present simulation suggests that the recirculation re-attaches approximately past half of the hole.

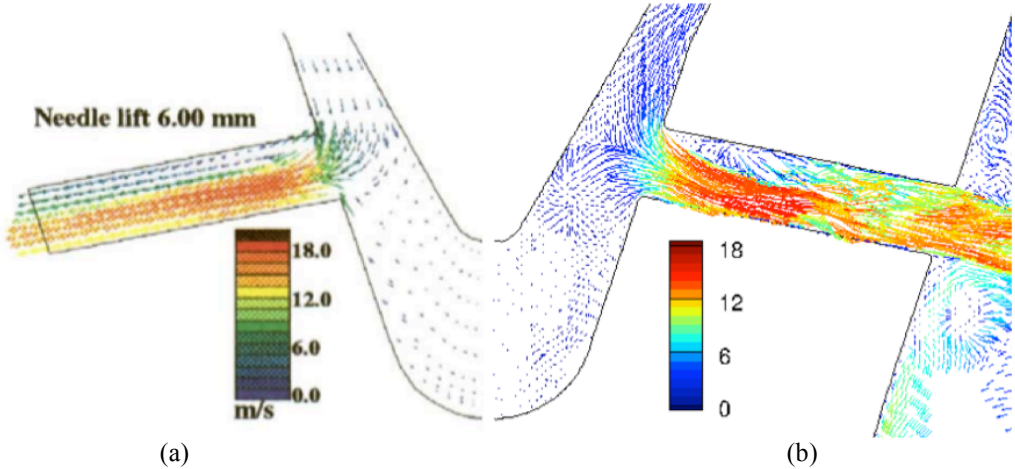


Figure 5. RANS velocity flow field from [5] (a) compared to the present calculation flow field (b).

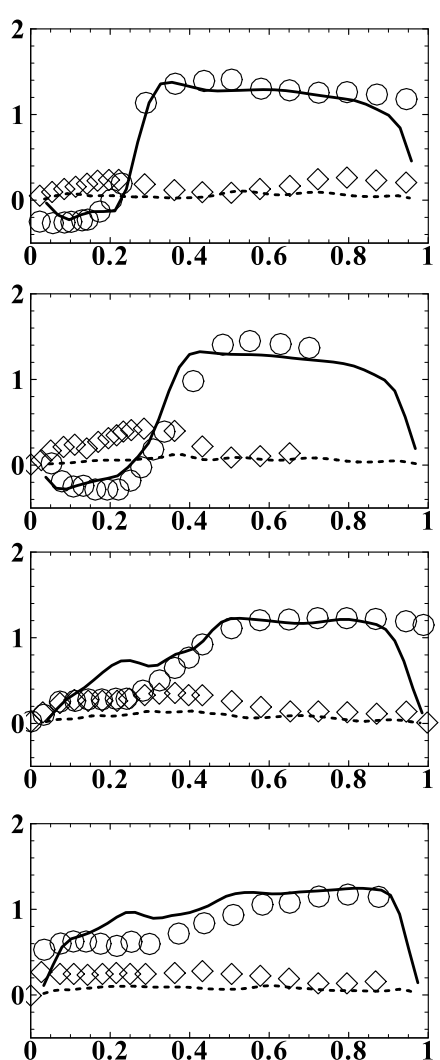


Figure 6. The circle and lozenge symbols are the mean and rms centerline values of velocity at four cross-sections along the injection hole. The continuous and dashed lines are the corresponding values from the simulation. From top to bottom: $x = 9.5, 10.5, 13.5$, and 16.5 .

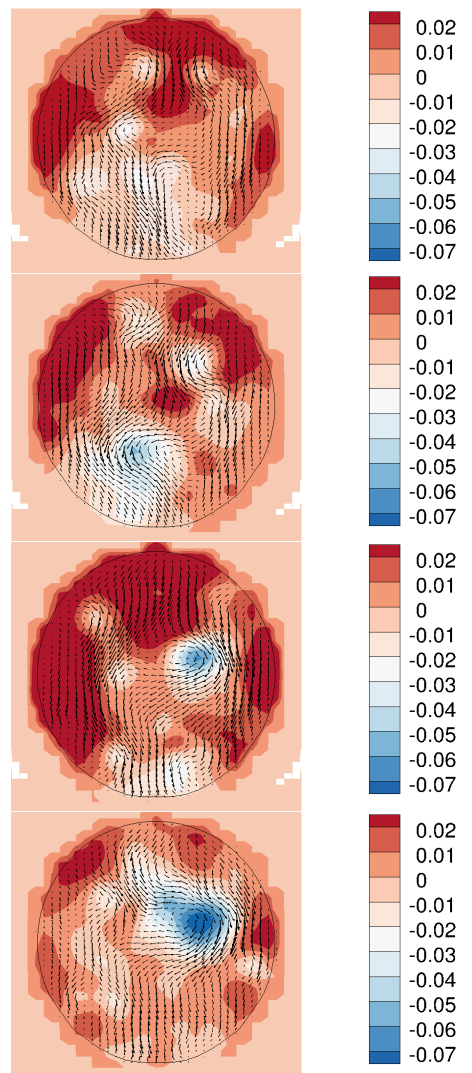


Figure 7. Slices through the injector's orifice 5 ms apart (from top to bottom). The pressure plot is in bar.

The mean and root mean square (rms) flow velocity (normalized by the mean orifice velocity) are compared to the LDV measurements in the plots of Figure 6. The values are taken at the four radial locations shown in Figure 3. We note that the measured recirculation zone closes less rapidly than in the simulation, but, overall, the velocity mean values compare favorably with the experiment. The measured rms values are, however, consistently larger than in the calculation, with the largest discrepancy in the $x = 10.5$ slice immediately outside of the recirculation zone (this rms peak is similarly lost in the RANS calculation from [5]).

The underestimate of velocity fluctuations is common to low order of accuracy simulations that attempt to capture the unsteadiness of turbulent flow. Similarly, the smaller thickness of the computed boundary layer compared to the experiment can be attributed to the lack of grid resolution at the walls. It is noted that the proposed approach cannot take advantage of grid stretching or, say, wall-aligned, prism layers to achieve better boundary layer resolution. The orifice diameter measures approximately 45 grid cells. For this $Re = 10,000$ case, a posteriori analysis indicates that the wall shear velocity, $u_s = (\tau_w/\rho)^{1/2} \sim 0.02$ m/s, corresponding to a location in wall units of the first point away from the wall of $r^+ = \Delta x u_s/v \sim 1$. As a comparison, the resolved simulation of a planar channel flow at $Re = 3,300$ is reported to require a grid spacing of at least 7, in grid units [13].

In Figure 7, the pressure fluctuations at the exit of the injection hole ($x = 20$ mm) are captured in snapshots taken 5 ms apart: the circular line in the plot is the intersection of the $\psi = 0$ iso-contour with the slicing plane. Note that the pressure fluctuations with respect to the section average are mostly positive in the upper half of the exit orifice, consistent with the lower velocity values there (see Figure 5b). Interestingly, negative pressure variations can occasionally be observed in the upper half (as in the bottom frame of Figure 7) due to unsteady vortex motion.

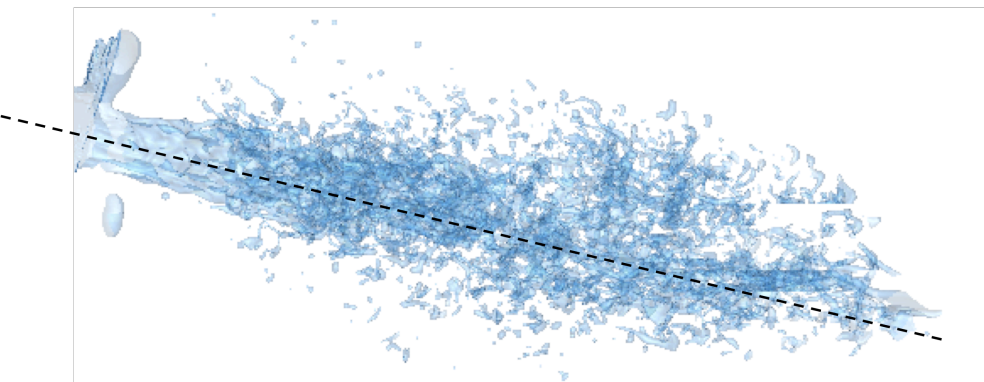


Figure 8. Spray snapshot with centerline (dash line) drawn from the orifice.

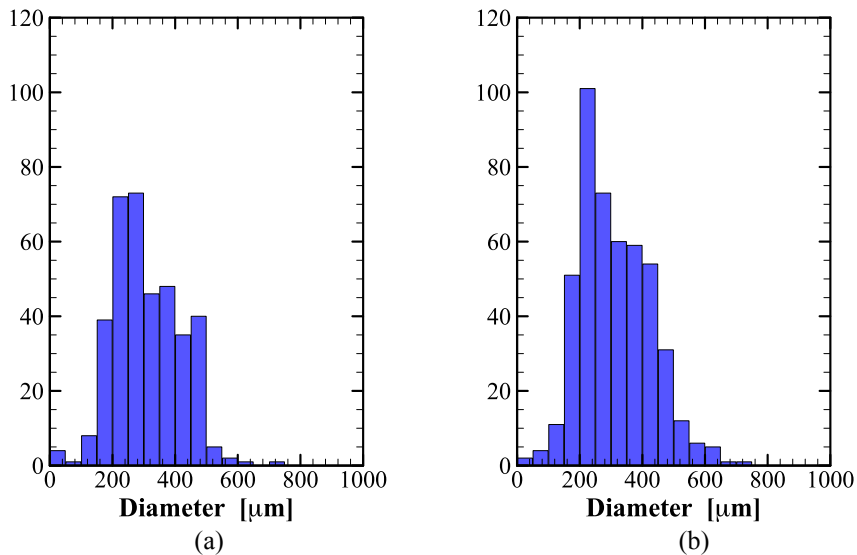


Figure 9. Droplet size distribution in the half the spray that is closer to the injector's tip (a) and farther away (b) at $t = 035$ ms.

We conclude by briefly examining how the spray is affected by the non-uniform inlet conditions, namely the occurrence of larger velocities in the bottom half of the orifice. The most apparent feature of the jet outside the nozzle is that it slightly bends upward, away from the tip of the injector; see Figure 8. In the plot, the liquid surface is rendered by the zero iso-contour of the liquid level-set; the dashed line marks the orifice axis. We consider the upper and lower half of the spray with respect to this line. As the faster side of the jet spreads less outwardly, it is interesting to interrogate the simulation about the corresponding drop size. Droplets are identified as isolated blobs from the $\phi = 0$ liquid surface. Their volume is translated into the effective diameter of the same-volume sphere, producing a histogram of diameter distribution. The one shown in Figure 9, for a snapshot taken at $t = 0.35$ ms, seems to suggest that the half of the spray that is closest to the tip of the injector has less droplets in the range from 200 to 400 μm . At this point, as with the other results reported in this section, more data would need to be collected before quantitative statements can be made.

Summary and Conclusions

A new simulation capability where internal and external flows can be calculated seamlessly across the injection hole is presented. The external liquid-gas interface can be handled by the combined level-set volume-of-fluid (CLSVOF) method, whereas the solid wall boundary is represented by a second level-set function on the same Cartesian, block-structured grid. This approach shifts the burden of handling arbitrarily complex injector geometries to the much simpler task of obtaining a tessellation of the injector surfaces, sidestepping altogether volume mesh generation. While this approach is only first-order accurate, moving parts of the injector and contacts – such as they occur when the needle shifts during a Diesel injector operation cycle – are trivial to include, since they simply require a level-set recalculation. It is furthermore conceivable that the deformation of the solid wall can be provided by a coupled Finite Element solver; see Ref. [14] for an example of such coupling.

Further work will address issues associated with real-size injectors, such as cavitation and compressibility of the liquid phase. In the internal flow portion of the calculation, an outstanding challenge remains the capability to provide a realistic turbulent flow at high Reynolds numbers. In the external flow, the difficulty remains to find well-characterized spray data that can be used for validation, so that internal geometry effects can be fully assessed.

Acknowledgements

Support by Sandia National Laboratories' LDRD (Laboratory Directed Research and Development) is gratefully acknowledged. Sandia National Laboratories is a multi-program laboratory managed and operated by Sandia Corporation, a wholly owned subsidiary of Lockheed Martin Corporation, for the U. S. Department of Energy's National Nuclear Security Administration under contract DE-AC04-94AL85000. A particular thank to Sarah Scott for her relentless effort at post-processing the simulation data.

References

- [1] Li, X., Arienti, M., Soteriou, M., and Sussman, M., AIAA-2010-0210, 48th AIAA Aerospace Sciences Meeting 2010.
- [2] Arienti, M., Li, X., Soteriou, M. C., Eckett, C. A., Sussman, M., and Jensen, R. J., to appear in *J. Prop. and Power*.
- [3] Arienti, M., Pan, W., Li, X., and Karniadakis, G., *J. Chem. Phys.* 134: 204114 (2011).
- [4] Giannadakis, E., Gavaises, M., and Arcoumanis, C., *J. Fluid Mech.* 616: 153-193 (2008).
- [5] Arcoumanis, C., Gavaises, M., Nouri, J. M., Abdul-Wahab, E., Horrocks, R. W., *SAE Technical Series*, 980911, 1998.
- [6] Chang, Y.C., Hou T.Y., Merriman, B., and Osher, S., *J. Comput. Phys.* 124: 449-464 (1996).
- [7] Duffy, A., Kuhnle, A., and Sussman, preprint at <http://www.math.fsu.edu/~sussman/MGAMR.pdf>
- [8] Sussman, M., Smith, K.M., Hussaini, M.Y., Ohta M. and Zhi-Wei. R., *J. Comput. Phys.* 221(2), 469-505 (2007).
- [9] Stewart, P.A., Lay N., Sussman, M., and Ohta M., *J. of Scientific Computing*, 35(1), 43-61 (2008).
- [10] Dommermuth, D., Sussman, M., Beck, R., O'Shea, T., and Wyatt, D., in Proceedings of the Twenty Fifth Symposium on Naval Hydr., St. Johns, New Foundland and Labrador, Canada, 2004.
- [11] Calhoun, D., *J. Comput. Phys.* 176: 231-275 (2002)
- [12] Dennis, S. C. R., and Chang, G., *J. Fluid Mech.* 42: 471 (1970).
- [13] Kim, J., Moin, P., and Moser, R., *J. Fluid Mech.* 177:133-166 (1987).
- [14] Arienti, M., Hung, P., Morano, E., and Shepherd, J.E., *J. Comp. Phys.* 185:213-251 (2003).